Subpixel Resolution Schemes for Multiphase Flows

by

Michael R Brady

Thesis submitted to submitted to the faculty of the Virginia Polytechnic Institute and State University in partial fulfillment of the requirements for the degree of

Master of Science

in

Engineering Mechanics

Graduate Advisory Committee:
Dr. Pavlos Vlachos (Chairman) – Mechanical Eng. Dept. at VPI&SU
Dr. Demetri Telionis – Engineering Science and Mechanics Dept. at VPI&SU
Dr. Roe Hoan Yoon – Mining Eng. Dept. at VPI&SU

October 20, 2006
Blacksburg, Virginia

Keywords: Particle Image Velocimetry, Particle Tracking Velocimetry, Spray Dynamics, Multiphase flows, Subpixel Resolution

Subpixel Resolution Schemes for Multiphase Flows

Michael R Brady

Abstract

This effort explores novel sub-resolution particle center estimation algorithms for Digital Particle Tracking Velocimetry (DPIV). The errors of these new methods were classified through Monte-Carlo simulations. These schemes provide direct measurements of the apparent particle image diameter and the subpixel position. The new methods significantly reduce the bias error due to pixel discretization, thus reducing the total error in the position and sizing measurement compared to the classic three point and least squares Gaussian estimators. In addition, the accuracy of the least-squares fits were essentially independent of the true particle diameter and significantly reduced the particle position error compared with current estimation schemes. The results of the Monte Carlo simulations were validated in a high pressure spray atomization experiment.

Table of Contents

1 Introduction..... 1

2 Particle Sizing Methodology..... 5

2.1 Three Point Gaussian Fit..... 6

2.2 Four Point Gaussian Estimator..... 7

2.3 Least Squares Gaussian Fit..... 9

2.4 Center of Mass..... 10

2.5 Pixel Counting..... 10

2.6 Continuous Four Point Fit..... 11

2.7 Continuous Least Squares Gaussian Fit..... 12

3 Monte Carlo Simulations..... 13

4 Results of Monte Carlo Simulations..... 15

4.1 Dependence on Point Selection Schemes..... 15

4.2 Peak Locking..... 16

4.3 Diameter Analysis..... 17

4.4 Position Analysis..... 19

5 Experimental Comparison..... 25

5.1 Experimental Setup..... 25

5.2 Experimental Results..... 26

6 Conclusions..... 29

References..... 30

List of Figures and Tables

Figure 1 Saturated pixels on a CCD and CMOS image sensor…… 2

Figure 2 - Examples of an acceptable set of points …… 8

Figure 3 - Inherent error due to pixel discretization…….. 11

Figure 4 – Point selection methods for least square fits……16

Figure 5 Mean Error of x coordinate as a function of true x position, σ_n =0, d=1.5 pixels…… 18

Figure 6 Mean Error of diameter as a function of true x position, σ_n =0, d=1.5 pixels..…18

Figure 7 – Diameter Error, σ_n =0, 8 bit, (a) top, total error; (b) center, bias error; (c) bottom, RMS error……...…… 21

Figure 8 – Diameter Error, σ_n =0, 12 bit, (a) top, total error; (b) center, bias error; (c) bottom, RMS error……...…… 21

Figure 9 – Diameter Error, σ_n =4, 8 bit, (a) top, total error; (b) center, bias error; (c) bottom, RMS error……...… 22

Figure 10 – Total Diameter Error, σ_n=4, 12 bit……22

Figure 11 – Total Diameter Error, σ_n=8, 8 bit……..…… 22

Figure 12 – Total Diameter Error, σ_n=12, 8 bit…… 22

Figure 13 – Position Error, σ_n =0, 8 bit, (a) top, total error; (b) center, bias error; (c) bottom, RMS error……...…… 23

Figure 14 – Position Error, σ_n =0, 12 bit, (a) top, total error; (b) center, bias error; (c) bottom, RMS error……23

Figure 15 – Position Error, σ_n =4, 8 bit, (a) top, total error; (b) center, bias error; (c) bottom, RMS error……...…… 24

Figure 16 – Total Position Error, σ_n =4, 12 bit……..…… 24

Figure 17 – Total Position Error, σ_n =8, 8 bit…… 24

Figure 18 – Total Position Error, σ_n =12, 8 bit……...… 24

Figure 19– Measurement location of spray……...…… 26

Figure 20 – Comparison of probability density of particle diameters……..…… 27

Table 1 – mean and standard deviation of particle diameters……...…… 28

1 Introduction

Multiphase flows are encountered in a variety of industrial applications. Some typical examples are the atomization of droplets in sprays, bubbly flows, flotation, and a variety of applications in the grain industry. The interaction of dispersed phases with the flow or with each other is not well understood and there is a need for robust diagnostic tools to simultaneously quantify the size and velocity characteristics of the different phases. Particularly in the design of more efficient spray atomizers, the flow diagnostics method needs to be time resolved and to provide sufficient spatial resolution in order to understand the dynamics of the system (Nishino et al. 2000; Bachalo 1994).

Phase Doppler Analyzers (PDA) is the most common tool that can deliver simultaneous velocity and size measurements (Fan et al. 1997) over a large range of particle sizes. PDA as well as other interferometer based techniques have proven to be reliable for size and velocity characterization. The major limitation of interferometer based methods is that they require the assumption of a spherical droplet (Black et al. 1996; Jones 1999). In addition, PDA is a point measurement technique therefore requiring elaborate traversing, phase triggering and ensemble averaging in order to adequately resolve the spatio-temporal variation of the flow

Particle Tracking Velocimetry (PTV) requires the sub-pixel determination of the particle center (Guezennec and Kiritsis 1990). For multiphase flows, hybrid schemes (Cowen and Monismith 1997) combining PIV and PTV have been used and appear advantageous in multiphase flows. Most optical diagnostic methods commonly employ different types of optical filtering or image segmentation in order to separate different phases in the flow (Khalitov and Longmire 1999, Boedec and Simoens 2001). In the case of multiphase flows when the velocity is estimated using cross-correlation with poly-dispersed distribution of particles or in the presence of droplets or bubbles, the measurement is significantly biased towards the velocities of the large particles. Therefore, when there is a large range of particle sizes, particle tracking is ideal.

Sizing directly from the recorded images is conventionally performed using pixel counting algorithms (Wang el al. 2002). Pixel Counting usually applies a threshold filter and then finds an equivalent diameter of the binarized image using the assumption of a spherical particle. Kadambi et al. (1998) modified this method by using an intensity weighted standard deviation algorithm. These approaches are highly susceptible to errors due to thresholding and other image pre-processing tasks since the edges of the particle are difficult to determine

accurately. In addition, they do not take advantage of the Gaussian intensity profile of the particle image.

The accuracy of the estimator to characterize a particle that contains saturated pixels is an important parameter that has not received enough attention. Digital media, CCD (Charge Coupled Device) or CMOS (Complementary Metal Oxide Semiconductor) sensors often contain saturated pixels due to their limited depth of resolution, and energy well capacity. Overexposure of a pixel to high intensity light results in an alias of the particle image. In the case of CCD sensors, this is usually coupled with a blooming effect where the intensity in excess leaks to the neighboring pixels thus altering the true Gaussian shape of the particle image. To demonstrate the effect of particle saturation, Figure 1 shows the true Gaussian intensity profile of a particle (line), along with the expected measured intensities from a CCD (light bars) and CMOS (dark bars) image sensor. It is important to note that despite the author's research, we were unable to find an accepted model to quantitatively simulate the leakage. CMOS sensors due to their pixel isolation capability will cut-off the light intensity at the maximum resolvable level, thus preventing any leakage. Although CCD sensors used for scientific applications generally offer anti-blooming filters, there is always extra charge that can spill-over into the neighboring pixels and compromise the image. In addition, for CCD sensors, the coupling of the pixels and the information readout process further amplify the effect. For multiphase flows with a substantial size difference between the phases, the field of view will contain saturated pixels even if optical

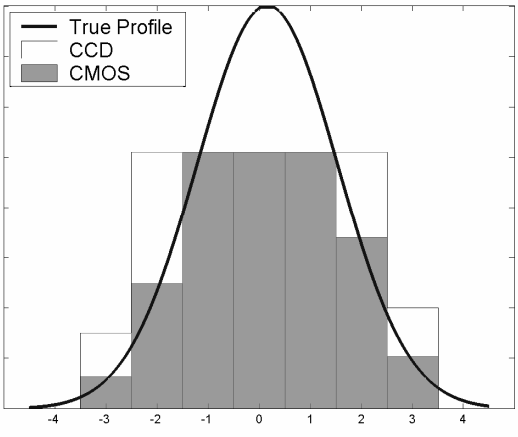

Figure 1 - Saturated pixels on a CCD and CMOS image sensor

filtering is used. The ability to accurately quantify particle images containing saturated pixels is important in order to maximize the measurement range and accuracy.

Image based sizing and velocity measurements of particles from DPIV recorded images are hampered by the pixel resolution of the recording digital media and the limited accuracy of the sub-resolution estimation schemes. This study represents our effort to overcome the limiting capabilities of the conventional estimation schemes and deliver accurate particle center and diameter measurements over a wide range of particle diameters.

New position and size estimation algorithms are developed to overcome some of the limitations discussed in the previous paragraphs. The objective is to reduce the errors in the position and the diameter measurements. We introduce three new fitting schemes that consist of two variations of a four point Gaussian estimator and an alternative local least-squares (LLS) fit. The improvements stem from addressing the limitations of the three-point estimation schemes. Specifically, the developed schemes account for the error associated with the pixel discretization, and remove the effect of saturated pixels. These will be discussed in greater detail in later sections. The developed schemes are compared with established methods such as center of mass, three-point Gaussian fit estimator and a least square fit method. These methods will also be experimentally compared with the well established method of particle sizing measurement, a Phase Doppler Analyzer.

Nomenclature

a_i = discrete intensity value

d = particle diameter

d_r= pixel resolution of recording medium

d_t = geometric image diameter

d_s =diffraction limited spot diameter

D_r = true particle position

D_m = measured particle position

E_{true} = RMS error with respect to true value

E_{mb} = mean bias error

E_{rms} = RMS error with respect to mean

f# = f-number of the lens

I_o = maximum intensity

M = magnification of image

(x_c,y_c) = particle center

(x_i,y_i) = pixel location for point i

λ = illumination wavelength

σ = standard deviation of Gaussian curve

σ_n = standard deviation of added noise level

2 Particle Sizing Methodology

The approaches presented herein follow the assumption that an axis-symmetric Gaussian shape can be used to approximate the intensity distribution of the light scattered from small particles. Lorenz-Mie theory provides the exact solution to the problem of scattering of light by a single homogeneous sphere, and relates the light scattering intensity to the true particle/droplet diameter. However, since the solution is difficult to apply for practical applications, the diameter can be approximated by geometrical optics principles. It has been shown that the Airy distribution of the point spread function from a diffraction limited lens can be very closely characterized as a Gaussian function (Adrian and Yao, 1985). .If the point spread function and the geometric image are Gaussian shaped, then the intensity distribution can also be closely approximated by a Gaussian. Also, the exposure time that depends on either the shutter of the high speed camera or the pulse duration of the laser, is very short compared to the particle velocity, thus avoiding non-spherical particle images and streaks in the extreme case.

The recorded particle image, d_t can be written in terms of the particle diameter, d, the diffraction limited spot diameter, d_s, and the resolution of the recording medium, d_r, as:

$$\mathbf{d_t}^2 = \mathbf{d_e}^2 + \mathbf{d_r}^2$$

$$\mathbf{d_e} = (\mathbf{M}^2\mathbf{d}^2 + \mathbf{d_s}^2)^{1/2} \qquad \textbf{(1)}$$

$$\mathbf{d_S} = 2.44(\mathbf{M}+1)\mathbf{f}\#\lambda$$

where M is the magnification, f# is the numerical aperture of the lens, and λ is the wavelength of a coherent monochromatic light source. Equation 1 represents the combined effects of the optical system's magnification and diffraction on the particle image when optical aberrations are not present. The geometric image diameter, d_t, and its subsequent estimation from various fitting schemes will be studied herein using artificially generated images. The back calculation of the true particle diameter is not addressed, Kadambi et al. (1998) examines the issues involved with the calculation of the true particle diameter, d from d_e.

Gaussian fitting schemes such as the three-point estimator and local-least squares estimator have been shown to provide reduced error in particle center estimation of the geometric image compared to more traditional methods such as center of mass (Udrea et al. 1996; Marxen et al. 2000, Willert and Gharib 1991). In addition, peak locking of the bias-error

was considerably reduced for the three point fit compared to the centroid approximation (Willert and Gharib, 1991). Therefore Gaussian fitting schemes will be the focus of this study.

The use of Gaussian fitting schemes for finding particle positions and correlation peaks has been very well documented. However, using the same schemes to find particle size has not been investigated comprehensively. Marxen et al. (2000) classified the measured particle diameter with the true diameter for a three point Gaussian estimator and a least squares estimator. Their results were significantly affected by preprocessing methods and errors in excess of 50% were reported. However, since this was not the primary focus of their study the sizing did not receive further attention. The various sizing and position estimation schemes used in the present analysis will now be described.

2.1 Three Point Gaussian Fit

The three-point Gaussian estimator is a one-dimensional approximation of the geometric particle image.

$$\mathbf{a_i = I_o e}^{-\frac{(\mathbf{x_i - x_c})^2}{2\sigma^2}} \tag{2}$$

The three independent variables: Io, σ, and x_c represent the maximum intensity, the Gaussian distribution standard deviation and the center position, respectively. If the three points chosen to solve these equations are the maximum intensity pixel, and the two neighboring pixels along the x-axis, then the standard three-point Gaussian estimator can be derived (Willert and Gharib 1991).

$$\mathbf{x_c = x_o + \frac{\ln a_{o-1} - \ln a_{o+1}}{2(\ln a_{o-1} + \ln a_{o+1} - 2\ln a_o)}} \tag{3}$$

The equation for finding y_c is equivalent, therefore five points are actually needed. The diameter measurement is directly related to the variance,

$$\sigma^2 = \frac{\ln \mathbf{a_{o+1}} - \ln \mathbf{a_o}}{(\mathbf{x_o - x_c})^2 - (\mathbf{x_{o+1} - x_c})^2} \tag{4}$$

The three point estimator is computationally fast and easy to implement. Its limitations are that it is a one-dimensional approximation thus when employed in 2-D it is practically a five point scheme that restricts the selection of points to the highest intensity pixel and its four neighbors. The three-point Gaussian fit does not allow discarding any pixels on the basis of their intensity, thus saturated pixels may be used in the measurement.

2.2 Four Point Gaussian Estimator

A four point estimator is now presented. The motivation behind this method was to overcome the limitations of the three-point Gaussian fit and allow determining the center and diameter of a particle when it contains saturated pixels. For this scheme, if saturated pixels exist, it is enforced that they do not contribute to the measurements. They are discarded and the measurements are then performed from the adjacent un-saturated pixels. Removing the saturated high intensity pixels from the calculation allows for the accurate estimation of the particle maximum intensity value and the Gaussian spread, thus reducing the overall error of the method. Finally, the method is truly two-dimensional and accounts for the diagonal pixels.

Consider the two-dimensional intensity distribution:

$$a_i = I_0 e^{\frac{(x_i - x_c)^2 + (y_i - y_c)^2}{2\sigma^2}} \tag{5}$$

We can solve for the four independent variables using the unsaturated intensities and coordinates at four points. The solutions for the center and variance are shown in Equations 6-8, and depend upon twelve constants defined as:

$$\begin{aligned}
\alpha_1 &= x_4^2(y_2 - y_3) + (x_2^2 + (y_2 - y_3)(y_2 - y_4))(y_3 - y_4) + x_3^2(y_4 - y_2) \\
\alpha_2 &= x_4^2(y_3 - y_1) + x_3^2(y_1 - y_4) - (x_1^2 + (y_1 - y_3)(y_1 - y_4))(y_3 - y_4) \\
\alpha_3 &= x_4^2(y_2 - y_1) + x_2^2(y_1 - y_4) - (x_1^2 + (y_1 - y_2)(y_1 - y_4))(y_2 - y_4) \\
\alpha_4 &= x_3^2(y_2 - y_1) + x_2^2(y_1 - y_3) - (x_1^2 + (y_1 - y_2)(y_1 - y_3))(y_2 - y_3)
\end{aligned}$$

$$\begin{aligned}
\gamma_1 &= -x_3^2 x_4 + x_2^2(x_4 - x_3) + x_4(y_2 - y_3)(y_2 + y_3) + x_2(x_3 - x_4^2 + y_3^2 - y_4^2) + x_3(x_4^2 - y_2^2 + y_4^2) \\
\gamma_2 &= x_1^2(x_3 - x_4) + x_3^2 x_4 + x_4(y_3^2 - y_1^2) - x_3(x_4^2 - y_1^2 + y_4^2) + x_1(-x_3^2 + x_4^2 - y_3^2 + y_4^2) \\
\gamma_3 &= x_1^2(x_2 - x_4) + x_2^2 x_4 + x_4(y_2^2 - y_1^2) - x_2(x_4^2 - y_1^2 + y_4^2) + x_1(-x_2^2 + x_4^2 - y_2^2 + y_4^2) \\
\gamma_4 &= x_1^2(x_2 - x_3) + x_2^2 x_3 + x_3(y_2^2 - y_1^2) - x_2(x_3^2 - y_1^2 + y_3^2) + x_1(-x_2^2 + x_3^2 - y_2^2 + y_3^2)
\end{aligned}$$

$$\beta_1 = \mathbf{x}_4(\mathbf{y}_2 - \mathbf{y}_3) + \mathbf{x}_2(\mathbf{y}_3 - \mathbf{y}_4) + \mathbf{x}_3(\mathbf{y}_4 - \mathbf{y}_2)$$
$$\beta_2 = \mathbf{x}_4(\mathbf{y}_3 - \mathbf{y}_1) + \mathbf{x}_3(\mathbf{y}_1 - \mathbf{y}_4) + \mathbf{x}_1(\mathbf{y}_4 - \mathbf{y}_3)$$
$$\beta_3 = \mathbf{x}_4(\mathbf{y}_1 - \mathbf{y}_2) + \mathbf{x}_1(\mathbf{y}_2 - \mathbf{y}_4) + \mathbf{x}_2(\mathbf{y}_4 - \mathbf{y}_1)$$
$$\beta_4 = \mathbf{x}_3(\mathbf{y}_2 - \mathbf{y}_1) + \mathbf{x}_2(\mathbf{y}_1 - \mathbf{y}_3) + \mathbf{x}_1(\mathbf{y}_3 - \mathbf{y}_2)$$

$$x_c = \frac{\ln(a_1)\alpha_1 + \ln(a_2)\alpha_2 + \ln(a_3)\alpha_3 + \ln(a_4)\alpha_4}{2(\ln(a_1)\beta_1 + \ln(a_2)\beta_2 + \ln(a_3)\beta_3 + \ln(a_4)\beta_4)} \tag{6}$$

$$y_c = \frac{\ln(a_1)\gamma_1 + \ln(a_2)\gamma_2 + \ln(a_3)\gamma_3 + \ln(a_4)\gamma_4}{2(\ln(a_1)\beta_1 + \ln(a_2)\beta_2 + \ln(a_3)\beta_3 + \ln(a_4)\beta_4)} \tag{7}$$

$$\sigma^2 = \frac{(x_4 - x_c)^2 + (y_4 - y_c)^2 - (x_3 - x_c)^2 - (y_3 - y_c)^2}{2(\ln(a_3) - \ln(a_4))} \tag{8}$$

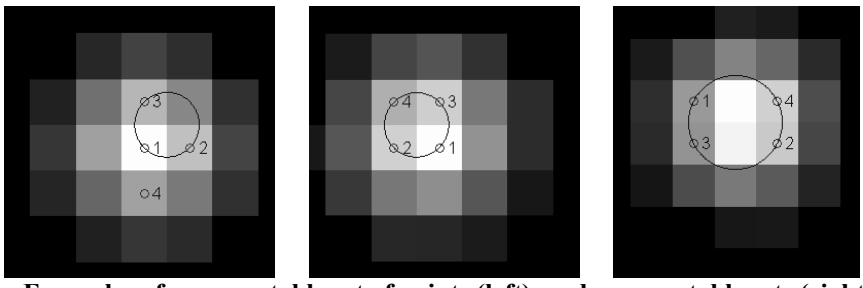

Figure 2 - Examples of an acceptable set of points (left), and unacceptable sets (right, center)

It must be noted that if any three points used in the four-point fit are the same as the ones used in the three point fit for the x-axis, then the solution to x_c, Equation 6, reduces to the three point estimator (Equation 3), and similarly for the y-axis form. It is also important to emphasize that the points selected for the four-point Gaussian estimation are not arbitrary and do not always yield a unique solution. The topology of the chosen points is paramount for the accuracy of the methodology and is determined by two additional conditions. The first condition depends upon the pixel coordinates (x_i,y_i) only and is independent of the intensities. Assuming that the previously stated requirement of unsaturated pixels is satisfied, by observation of equations 6 and 7, it is obvious that if the denominators of x_c and y_c go to zero, a solution cannot be determined. It is possible to have the entire sum in the denominator go to zero, but each term in the sum is independent and that solution is trivial. Therefore each term must individually go to

zero. Solving for $\beta_i=0$ yields the condition for all four points lying on the same line, which does not result to a solution in the four point fit and therefore must be avoided.

The second combination of points that does not yield a unique solution occurs if the four selected points all lie in a circle of any arbitrary center or radius. Assume any four points randomly located on a Gaussian shaped particle as shown in Figure 2 (left). If the fourth point belongs on the circle determined by the first three, then it can be shown that the solution to the particle center, Equation 6 and 7 reduce to the solution of the center of the circle intersecting the four points, and is independent of any intensity values. In addition, the variance in Equation 8 goes to zero. The mathematical proof of the above condition is apparent by inspection. Figure 2 shows examples of an acceptable (left) and unacceptable (center, right) groups of points.

The four-point Gaussian fit has the advantage over the three-point fit in that it is more flexible in selecting virtually any four of the pixels that satisfy the above conditions. Our practice showed that it is desirable to select pixels with high intensity and as close as possible to the maximum intensity pixel in order to reduce noise effects and minimize the error.

2.3 Least Squares Gaussian Fit

Local least-squares (LLS) have been used in the past as alternatives to the three point Gaussian fit. The position and the diameter can be estimated with sub-resolution accuracy using four or more pixels. The local least square fit is employed in this study by minimizing χ^2 described by Equation 9.

$$\chi^2 = \sum (a_i - I_o e^{-\frac{(x_i - x_c)^2 + (y_i - y_c)^2}{2\sigma^2}})^2 \qquad (9)$$

The minimization was performed using a Gauss-Newton algorithm. The least squares fit allows for selecting certain points while leaving others out with no topological constrains. Two methods of point selection were investigated in the Monte Carlo simulations presented later. First, the conventional 3x3 pixel area around the highest intensity pixel. This scheme was also investigated by Marxen et al. (2000). Second, all the available points with intensity over a certain threshold value are used in the calculation. This is the equivalent of a high pass threshold filter, and it is employed only for the larger particles in order to reduce excessive computational time.

2.4 Center of Mass

A center-of-mass (intensity weighted centroid) estimator was also investigated for providing a comparison baseline for the position estimators developed herein. This scheme provides the simplest approach for estimating the center and area of a particle. Although not limited by the size of a particle the accuracy of this method is significantly compromised by saturation and noise. Moreover, it is subject to severe peak locking effects, shown later, for particles with small diameters.

In addition to the error reduction, Gaussian schemes offer implementation advantages over the center of mass. The points used in each of the Gaussian fits either employ information very close to the highest intensity pixel, or provide the flexibility to choose the unsaturated points.

2.5 Pixel Counting

Pixel Counting gives an estimate of the apparent diameter of a particle with an easy to implement algorithm. The image is first preprocessed with a basic threshold filter therefore defining the particle boundary. The standard deviation of the intensity profile is then estimated and four standard deviations is taken to be the particle diameter (defined later). Pixel counting is computationally fast, however the method is very sensitive to preprocessing tasks that alter the boundary measurement of the particle.

Pixel Discretization-Integralchemes

The three and four point fits will contain an error even without the presence of noise sources due to the digital medium pixel discretization. This is illustrated in Figure 3 simplified into 1-D for explanation, showing the true intensity profile (curve) of a particle. This distribution is used to calculate the pixel intensity discrete values (bars). For any sensor, the discrete gray values are obtained by integrating the true intensity distribution over the photosensitive area of the pixel. The three point fit and the four point fit assume that the intensity value at the center of each pixel (point) is equal to the true intensity at that position instead of the total integrated intensity, thus fitting a curve through a biased value instead of the true value. This inherent

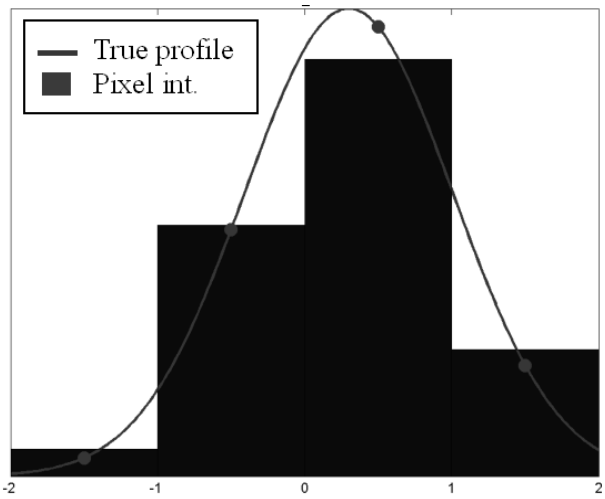

Figure 3 - Inherent error due to pixel discretization

error, as it will be shown later, can produce substantially large errors when calculating the particle position and diameter, especially for smaller particles.

2.6 Continuous Four Point Fit

Based on the above, an improved implementation of the four-point fit is now proposed. This is a continuous four point fit that eliminates the systematic error introduced by the pixel descretization. The continuous four point fit simply corrects for the pixel discretization by equating the integrated Gaussian profile over each pixel to the discrete gray value.

$$\mathbf{a_i} = \iint \mathbf{I_o} e^{-\frac{(\mathbf{x_i}-\mathbf{x_c})^2+(\mathbf{y_i}-\mathbf{y_c})^2}{2\sigma^2}} \mathbf{dydx} \tag{10}$$

Equation 10 cannot be solved in a closed-form, the expanded equations are shown in Equation 11 where Erf is the error function. Here x_i and y_i represent the position of the lower corner of each pixel, not the midpoint as in the Gaussian fits described above.

$$\mathbf{a_i} = \frac{\pi \mathbf{I_o} \sigma^2}{2} \left(\mathbf{Erf}\left[\frac{(\mathbf{x_i}-\mathbf{x_c})}{\sqrt{2}\sigma}\right] - \mathbf{Erf}\left[\frac{(\mathbf{x_i}+1-\mathbf{x_c})}{\sqrt{2}\sigma}\right]\right)\left(\mathbf{Erf}\left[\frac{(\mathbf{y_i}-\mathbf{y_c})}{\sqrt{2}\sigma}\right] - \mathbf{Erf}\left[\frac{(\mathbf{y_i}+1-\mathbf{y_c})}{\sqrt{2}\sigma}\right]\right) \tag{11}$$

The nonlinear equations were solved using a form of the Powell dogleg optimization routine as described by Powell (1970). The same rules for point selection used in the Four Point fit were employed to the Integrated Four Point fit.

2.7 Continuous Least Squares Gaussian Fit

The third novel sub-resolution scheme developed during this study is the integrated local least square fit. Similarly to the integrated four point fit, introduced above, this scheme improves the error by taking into account the discretization error of the individual pixels.

$$\chi^2 = \sum (\mathbf{a_i} - \iint \mathbf{I_o} \mathbf{e}^{-\frac{(\mathbf{x_i}-\mathbf{x_c})^2+(\mathbf{y_i}-\mathbf{y_c})^2}{2\sigma^2}} \mathbf{dydx})^2 \quad \textbf{(12)}$$

As with the standard least squares, χ^2 was minimized using a Gauss-Newton algorithm. The same analysis as the standard least square for the point selection was performed on the integrated least square.

3 Monte Carlo Simulations

Comprehensive comparisons between the methods described above were carried out. Monte-Carlo simulations using artificial images of particles with Gaussian shape intensity profiles, as defined by Equation 5, were generated with uniform random distribution for the values of I_o, x_c, y_c and σ. The diameter of a particle is defined as the e^{-2} intensity level of the Gaussian, which is equal to 4σ. The diameter was varied from 1.5 to 10.5 pixels, and the true particle center was randomly placed within a 1x1 pixel area. Since the recording medium for every exposure integrates over space as well as time to obtain the pixel's discrete gray value, the pixels were discretized by integrating the Gaussian curve over each pixel.

Two sources of noise were introduced. Normally distributed white background noise (positive values only) with a standard deviation, σ_n, ranging from 0-12 was added to each pixel intensity value. Once the intensity values were calculated, the entire gray value matrix was scaled so that the maximum intensity value of the discretized particle equaled the maximum intensity value allotted by the bit resolution (i.e. 255 for an 8-bit resolution). Each discrete gray value was then rounded to the nearest 8 or 12 bit number, simulating the second source of noise. Finally, a particle segmentation algorithm was applied to separate the particle from the white noise outside the particle boundary.

Each particle was produced independently; therefore the preprocessing performed on the images was minimal so as to not affect the results. A high pass threshold filter was the only preprocessing utilized. The threshold was equal to 2% of the maximum resolvable intensity value. A total of 50,000 particles were evaluated for each of the simulations, shown later, to provide sufficient sampling.

Following previous investigations (Fincham et al. 1997 and Marxen et al. 2000) we will separate the errors into a mean-bias error and an RMS error about the mean. Each particle was placed into a bin, based on its true diameter. Let D_r be the real position of the particle, and D_m the measured position. The position errors are as follows: The RMS error with respect to the true value (total or true error) is defined as:

$$E_{true} = \left[\frac{1}{N} \sum_{n=1}^{N} \left| D_r - D_m \right|^2 \right]^{1/2}$$

The difference between the actual displacements and the mean displacement is the mean bias error,

$$E_{mb} = \left| D_r - \frac{1}{N}\sum_{n=1}^{N} D_m \right|$$

The RMS error, revealing the deviation about the mean,

$$E_{rms} = \left[\frac{1}{N}\sum_{n=1}^{N} \left| D_m - \frac{1}{N}\sum_{n=1}^{N} D_m \right|^2 \right]^{1/2}$$

Note that the errors add up in quadrature, $E_{true}^2 \approx E_{mb}^2 + E_{rms}^2$. Also, the subtraction $D_r - D_m$ represents the distance between the true particle center and the measured particle center, therefore considers both the x and y errors. The error characterization for the measured diameters can be defined similarly.

4 Results of Monte Carlo Simulations

A comprehensive error comparison of the various fitting schemes will now be presented. The total, bias, and RMS errors of the measured diameter and measured position were investigated for varying white noise levels and bit resolutions. The effect of pixel selection was also investigated for both least square fits and both four point fits to determine their optimum conditions for implementation.

4.1 Dependence on Point Selection Schemes

First, it is important to characterize the fitting schemes that vary on the point selection. The standard least square and the continuous least square were compared, as stated earlier, using two separate point selection methods. The first method considers the 3x3 area centered at the highest intensity pixel while the second takes all available points above a threshold value of 5% of the dynamic range, i.e. for 8 bit images, a threshold of 13 was used. Figure 4 plots the total error for the position and the diameter for both least square fits and point selection methods for white noise level of σ_n=4, and 8 bit resolution. The position estimation using the 3x3 LLS, with some image preprocessing were investigated by Marxen et al. (2000). The total error for the position is shown in Figure 4(b). The results for the 3x3 scheme are in agreement with the ones presented by Marxen. Minor differences are attributed to the image prepossessing. The comparison between the methods clearly shows that the 3x3 scheme produces significant errors (for d>2 pixels) with respect to the method invoking all available points for the least square evaluation. At a diameter of 10 pixels, the error is 0.013 pixels for the least square fits with all points taken, versus a 0.075 pixel error for the 3x3 algorithm.

The diameter error in Figure 4(a) shows only a modest difference (2% maximum difference) in total error between the two point selection methods. However, the integrated least square performs substantially better than the standard least square for diameters less than 8 pixels. Because the total position error is so drastically affected by limiting the number of points employed, both estimators will use all available points in all subsequent simulations presented here.

The four-point fit and the integrated four-point fit also depend on optimizing the points to be used. A variety of point selection algorithms were considered such as selecting the points closest to the center (highest intensity) pixel, the points furthest away from the center, randomly

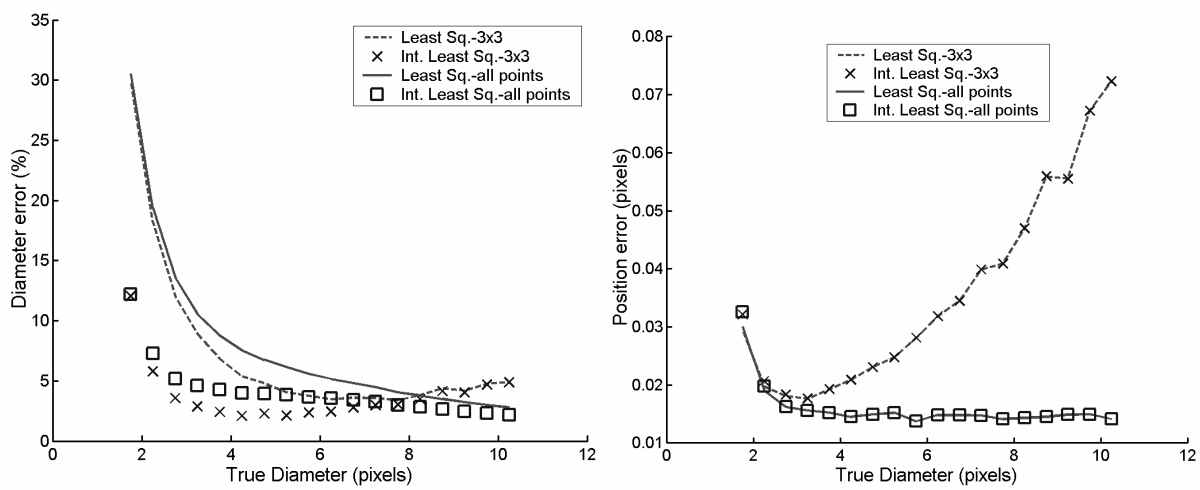

Figure 4 – Point selection methods for least square fits, (a)left, total diameter error (b) right, total position error, σ_n =4, 8 bit resolution

selected points, and uniformly spaced. It was determined that the total error in the diameter for both four-point fits was relatively insensitive to the point selection technique. However, the position error was affected more significantly by the point selection algorithm. The algorithm that performed best was the method using the highest intensity points closest to the center, probably because the highest intensity points contain the highest signal to noise ratio in the pixels. Therefore the two versions of the four-point fit will utilize this method when selecting points for the remainder of the simulations.

The effects of white noise intensity and bit resolution as a function of diameter and position within the pixel will now be discussed.

4.2 Peak Locking

Peak locking is an effect that causes the particle position measurement to be biased towards the integer pixel values (Huang et al. 1997; Udrea et al. 1996). Peak locking can also be described in mean error plots versus the true particle position as shown in Figures 5 and 6. Figure 5 shows that even with zero added noise the mean position error (x-direction only) variation is essentially zero at the extremes and in the center of the pixel. In contrast, methods accounting for the discretization error (continuous four point, continuous least squares) show essentially zero mean error without added noise, thus do not exhibit a peak locking effect. However with added random noise (case not shown), peak locking is observed.

The position error is subject to peak locking as described above. However, the mean diameter error is not a strong function of the true particle position, as shown in Figure 6. Again, the continuous Gaussian schemes eliminate the error entirely whereas the other schemes do contain pixel discretization error.

Subpixel position of a particle is not generally a controllable quantity; therefore peak locking may not be removed or minimized. This is in opposition to the case of the particle diameter, which can be a controllable quantity based on the optical configuration and may be adjusted to minimize the error of an experiment. The error as a function of true particle diameter will now be discussed.

4.3 Diameter Analysis

As explained above, pixel discretization introduces an error to the conventional sub-pixel resolution schemes even without the presence of noise sources. Figure 6 shows the effect pixel discretization has on the various fits with 8-bit resolution and no random noise (8 bit, σ_n =0). It is clear from the bias error plot, Figure 6, that the pixel discretization creates a mean error for all of the non-continuous fits (least square, three point, four point) of up to 20% (d=2 pixels). The integrated four-point and integrated least square are clearly immune to the discretization error. Also, the error created from pixel discretization is only significant for small diameter particles as seen by the convergence of all the fitting schemes at high diameters (d>8).

The effect of bit resolution can be evaluated by comparing Figures 6 and 7. Figure 7 (12 bit, σ_n =0) clearly shows a suppression of RMS error, therefore bit resolution, is increasing the random error in the 8-bit case and is almost completely suppressed by 12-bit resolution. Further examination of the RMS errors shows that the two least-square fits have approximately the same performance indicating a relative immunity to errors created from bit resolution. Moreover, a comparison of the total error plots, Figures 7(a) and 8(a) show that pixel discretization is significantly more dominant source of error than bit resolution since the bias errors from the non-integrated estimators dominate the total error plots by one order of magnitude.

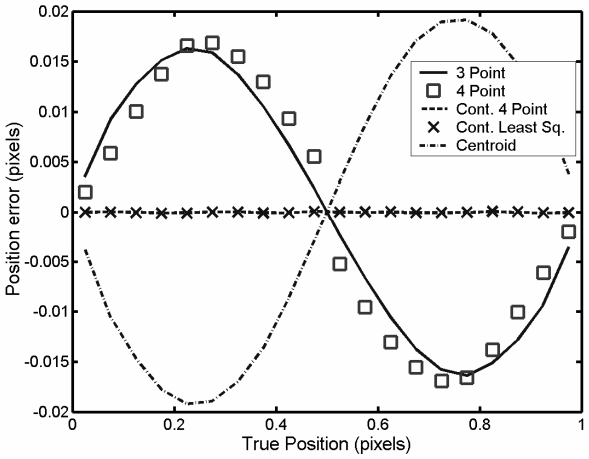

Figure 5 Mean Error of x coordinate as a function of true x position, σ_n =0, d=1.5 pixels

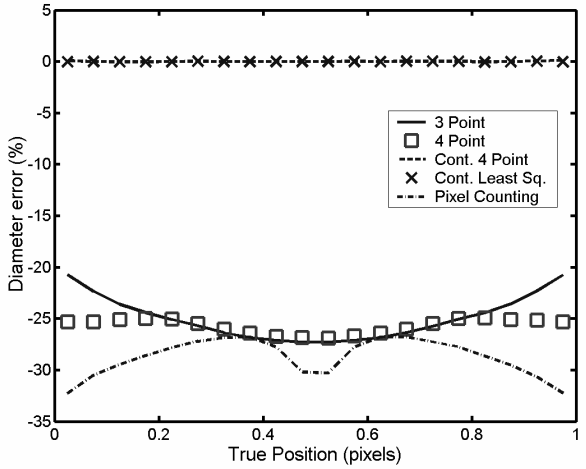

Figure 6 Mean Error of diameter as a function of true x position, σ_n =0, d=1.5 pixels

It is not practical to assume that particle images will exactly comply to a Gaussian profile due to random noise sources; therefore the addition of random white noise will now be investigated. Figure 9 shows the error for σ_n =4. The three-point, four-point, and integrated four point fits all possess local minimum total error values within the diameter range. The three point and four point fits both had minimum total error values at 5.5 pixels diameter and the integrated four-point fit had a minimum value at 4 pixels. The continuous four point fit and the continuous least squares perform significantly better than the other three methods, i.e. the total errors in calculated diameter are approximately 7% and 6.5% (d=2 pixels) for the Integrated Least

Squares and Integrated Four-point fits, respectively, compared to about 18% for the non-integrated estimators.

A comparison of Figures 9(a) and 10 shows no significant difference in the total error from 8 to 12 bits in the presence of a small noise level (σ_n=4). It is reasonable to assume that random noise and pixel discretization are the dominant sources of error in the calculation of particle diameter, while bit resolution plays a minimal role in the presence of even a small amount of random noise.

Higher noise levels of σ_n=8 and σ_n=12 are shown in Figures 11 and 12 respectively. The continuous four point fit had the least total error for diameters less than 5 pixels, and the continuous least squares had a lower total error for d>5 pixels for both noise levels. Over the entire diameter range (1.5-10.5 pixels), the newly proposed continuous least square method consistently outperformed the standard least square and had the lowest average total error. The continuous four point fit outperformed the three and four point fits at diameters less than 6 pixels over all noise levels due to the suppression of the bias error in the discretization process. At higher noise levels (σ_n>8), the three point fit performed more accurately than both four point fits. The total error for the four point and integrated four point fits was 24% versus 18% for the three-point fit (d=10 pixels, σ_n=8). Therefore, in the presence of extremely high noise levels where the particle image significantly deviated from its Gaussian shape, the gains in performance of these new schemes over the widely used three point fit are not significant for the diameter calculation.

4.4 Position Analysis

The position error is related to the accurate measurement of the particle tracking velocity. Position error, without the presence of random noise is shown in Figures 13 and 14. Figure 13 demonstrates that the continuous fits do not provide any advantages over the others for diameters greater than 2.5 pixels. However, for diameters less than 2.5 pixels, the integrated fits offer a significant advantage. That is to say at d=1.75 pixels, the total error in the continuous least squares fit offers approximately an 80% reduction in position error versus the standard least squares, and the continuous four point fit offers a 70% reduction over the four-point fit. However, at d=3 pixels, the continuous least squares converges with the standard least squares

and the continuous four point converges with the four point fit. Therefore pixel discretization contributes more significant error in the calculated diameter, as stated above, than it does in the calculated position. More importantly however, the total errors for both least squares fits are essentially independent of the true diameter for diameters larger than 3 pixels, remaining constant at 0.0015 pixels.

A comparison of the total errors in Figures 13 and 14 demonstrates that, without the presence of random noise (σ_n=0), a 12 bit resolution improves the error of each of the fits. However, with a small amount of added white noise (σ_n=4), the total errors are unaffected for the 8 (Figure 15(a)) and 12 (Figure 16) bit cases.

Further examination of the total position error reveals that at higher noise levels of σ_n=8 and 12, the four point fit converges with the continuous four point fit and the standard least squares converges with the continuous least squares. Therefore white noise is the dominant source of position error while pixel discretization and bit resolution are not significant. In addition, over the entire range of noise levels and particle diameters, both least squares fits are essentially independent of particle diameter and offer a significant advantage over the remaining fits. It should also be noted that the total error in the three point fit, for all white noise levels, is comparable to that reported by Marxen et al. (2000).

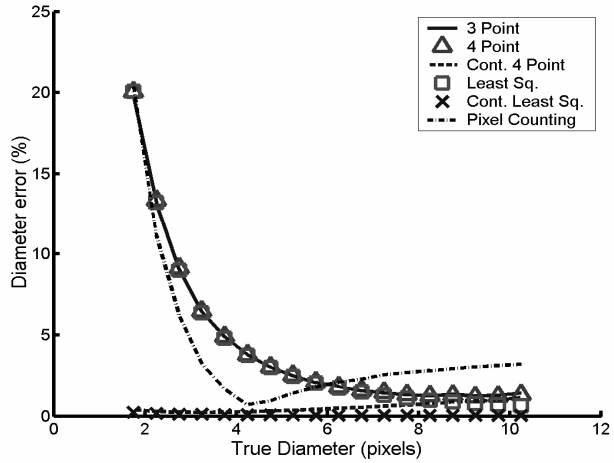

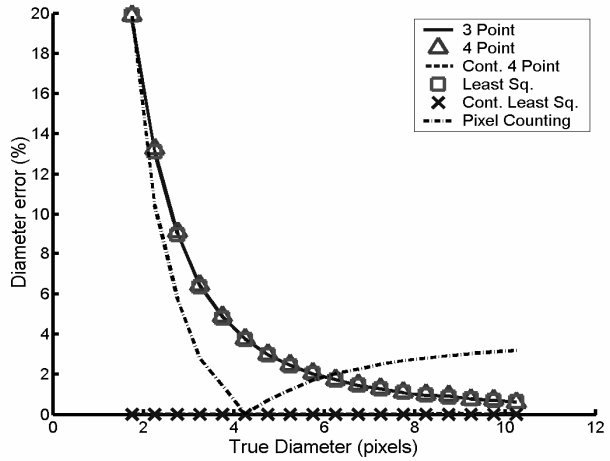

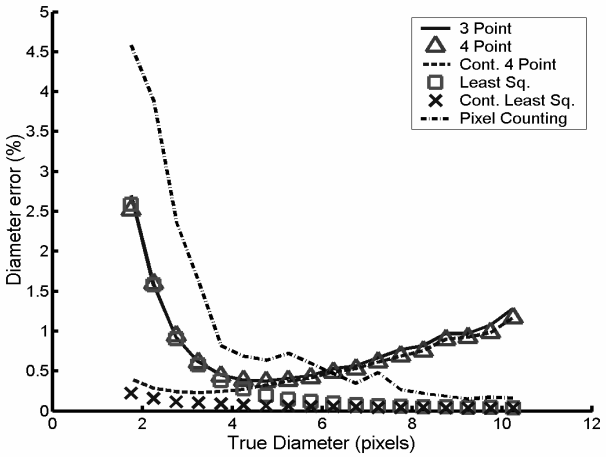

Figure 7 – Diameter Error, σ_n =0, 8 bit, (a) top, total error; (b) center, bias error; (c) bottom, RMS error

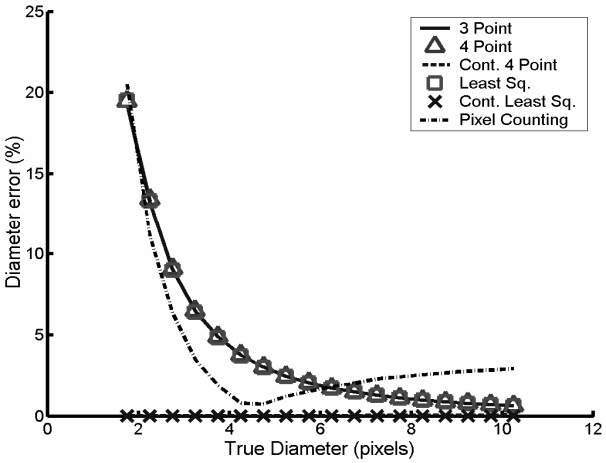

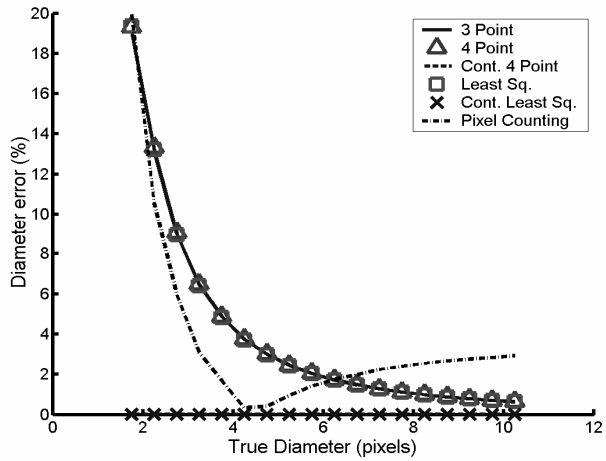

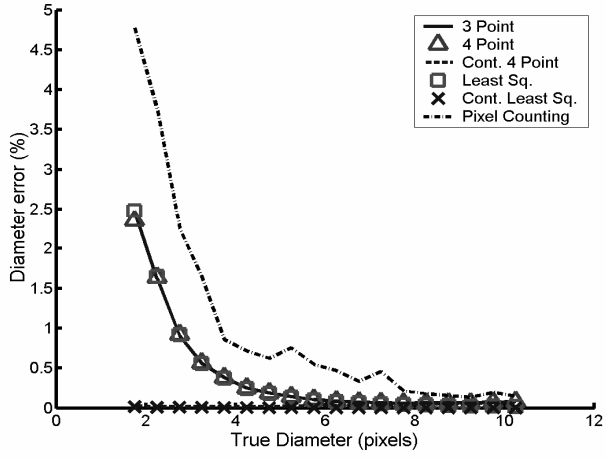

Figure 8 – Diameter Error, σ_n =0, 12 bit, (a) top, total error; (b) center, bias error; (c) bottom, RMS error

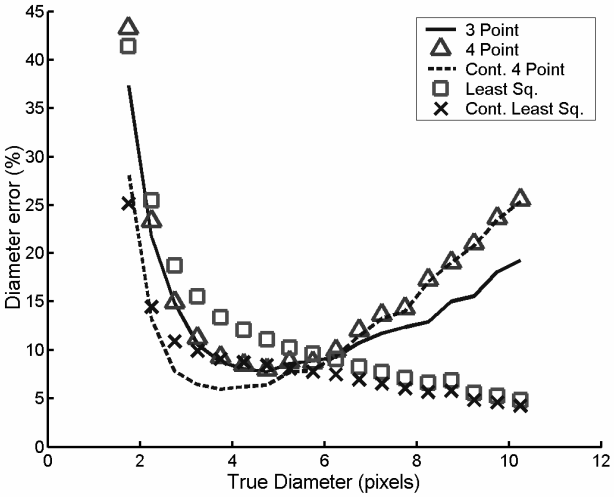

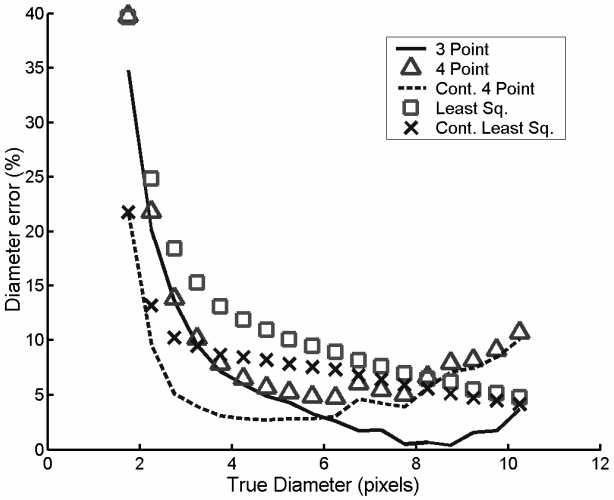

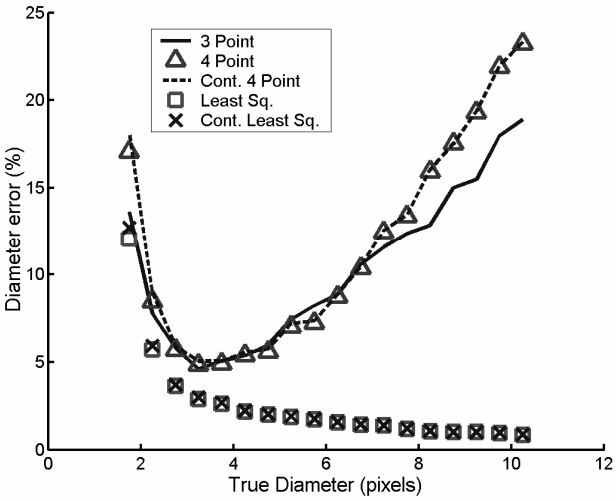

Figure 9 – Diameter Error, σ_n =4, 8 bit, (a) top, total error; (b) center, bias error; (c) bottom, RMS error

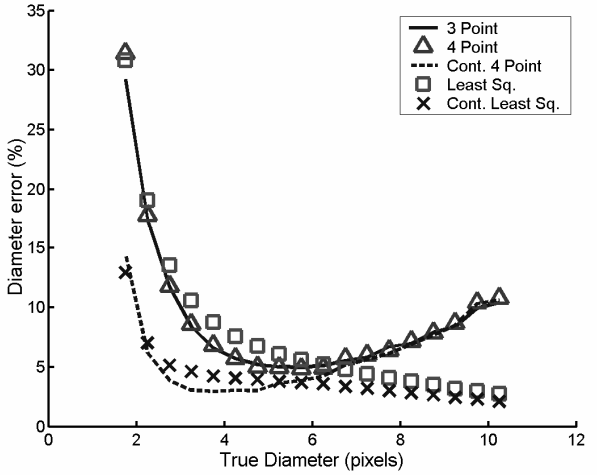

Figure 10 – Total Diameter Error, σ_n=4, 12 bit

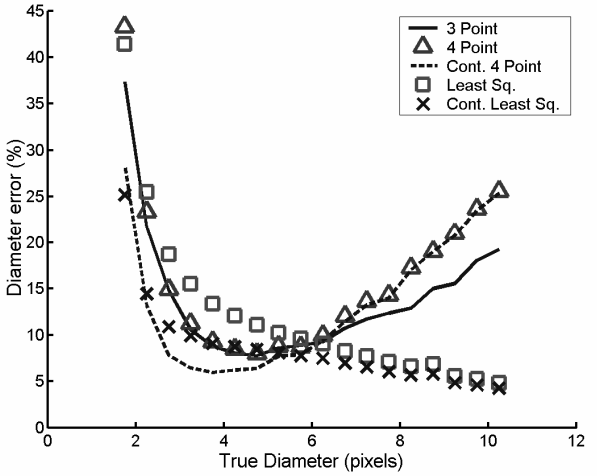

Figure 11 – Total Diameter Error, σ_n=8, 8 bit

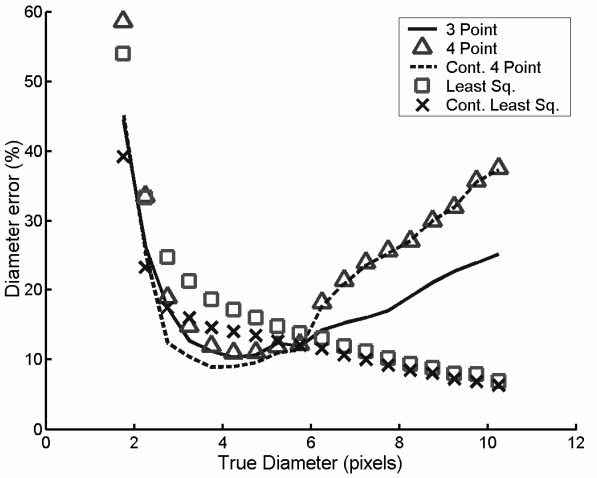

Figure 12 – Total Diameter Error, σ_n=12, 8 bit

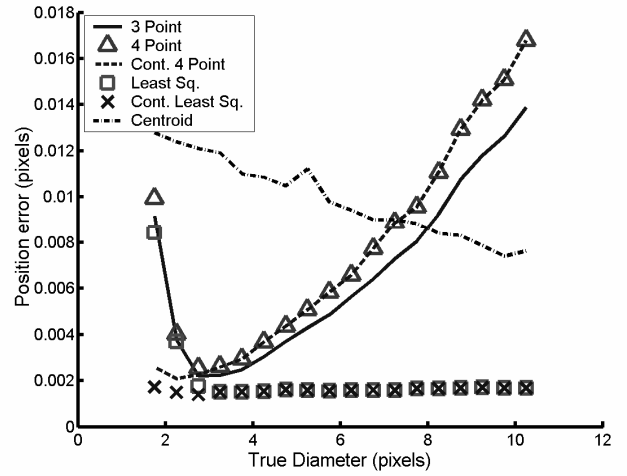

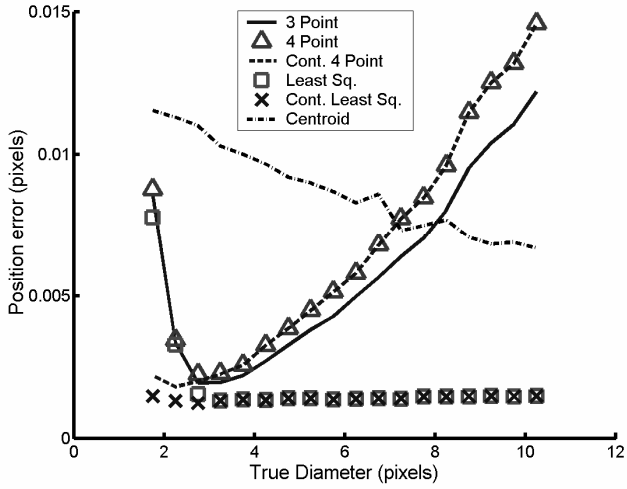

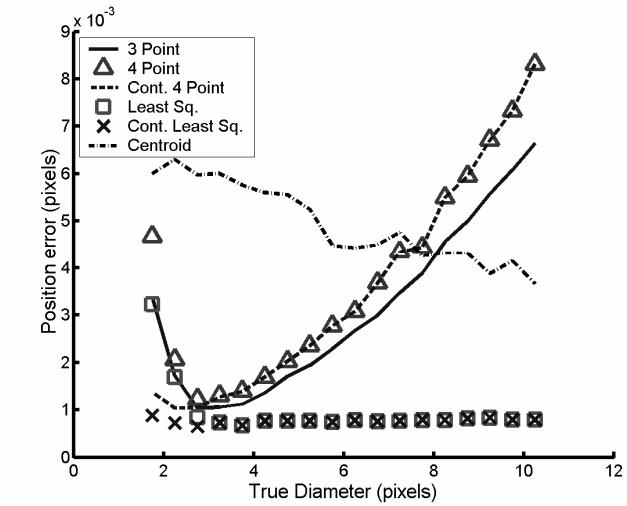

Figure 13 – Position Error, σ_n =0, 8 bit, (a) top, total error; (b) center, bias error; (c) bottom, RMS error

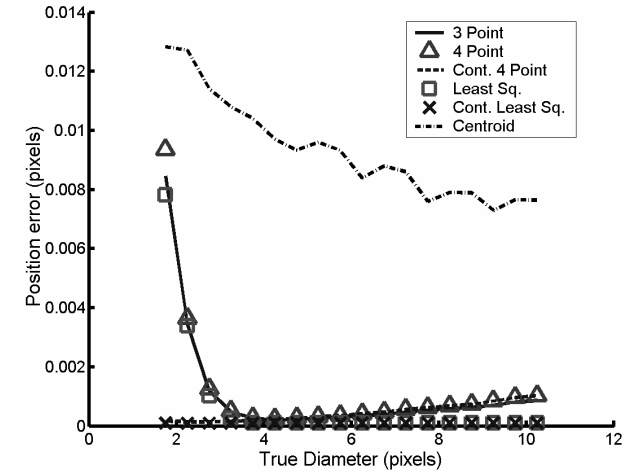

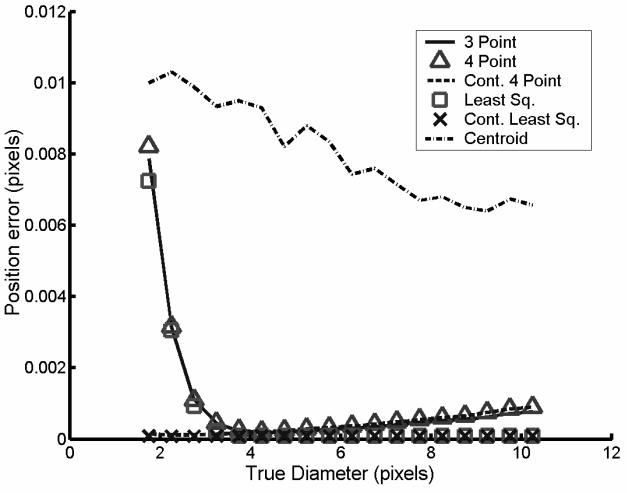

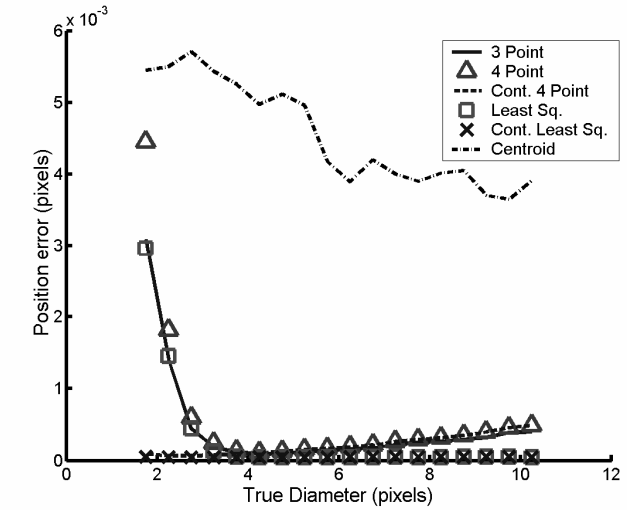

Figure 14 – Position Error, σ_n =0, 12 bit, (a) top, total error; (b) center, bias error; (c) bottom, RMS error

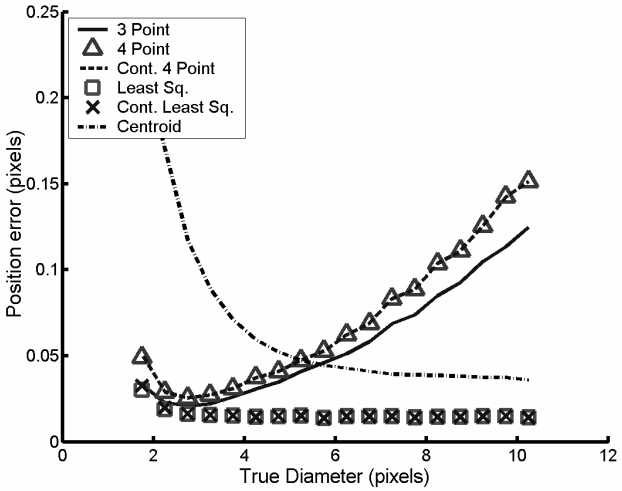

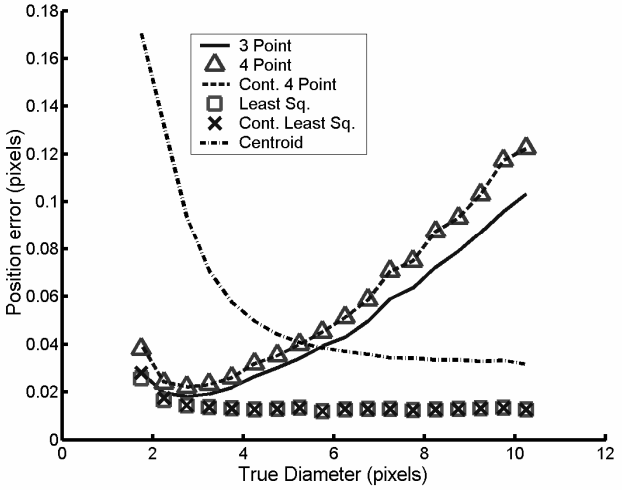

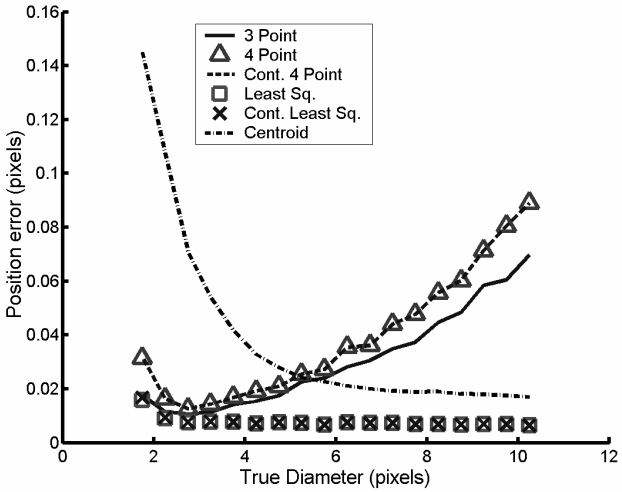

Figure 15 – Position Error, σ_n =4, 8 bit, (a) top, total error; (b) center, bias error; (c) bottom, RMS error

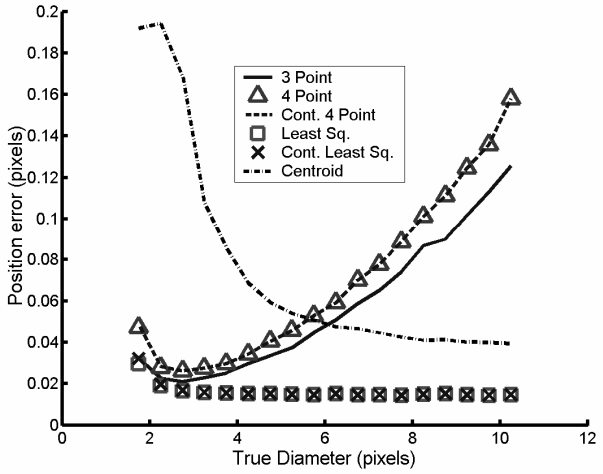

Figure 16 – Total Position Error, σ_n =4, 12 bit

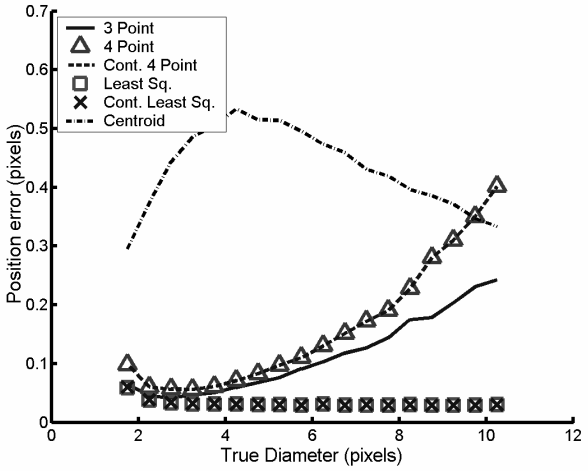

Figure 17 – Total Position Error, σ_n =8, 8 bit

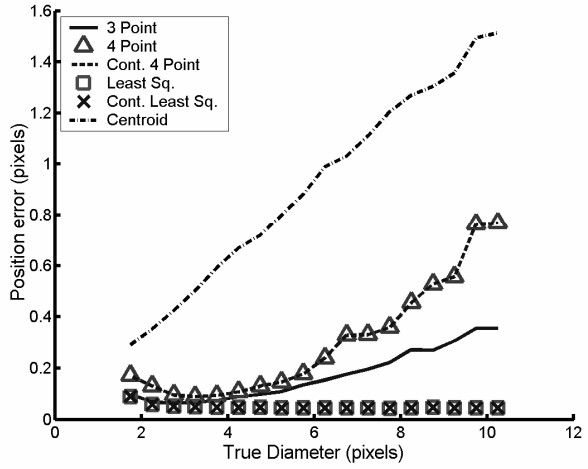

Figure 18 – Total Position Error, σ_n =12, 8 bit

5 Experimental Comparison

A high pressure spray experiment was set up to determine the effectiveness of the schemes presented above. The image based methods were compared to an additional set of measurements taken with a Phase Doppler Analyzer (PDA). Phase Doppler analyzers are an established method for determining particle diameters and velocities. Phase Doppler Anemometry (PDA) is the extension of the widely used non-intrusive particle velocity measurement technique known as Laser Doppler Anemometry (LDA). The method falls into non-imaging, single particle counter category. It uses light scattering interferometry and simultaneously measures size and velocity of spherical droplets. The method can also be used to provide volume flux, trajectory drop angle and time-resolved diagnostics of sprays. The measurements are dependent upon the wavelength of the scattered light from the droplets. The method was originally developed by Bachalo and Hauser (1984) and is now considered a benchmark technique for drop sizing and velocity measurement needs for most two phase flow research. These PDA measurements were taken in tandem with the image based Time Resolved Particle Image Velocimetry (TRPIV) measurements.

5.1 Experimental Setup

A one-dimensional Phase Doppler Analyzer from DANTEC Measurement Technology was used to measure the spray droplet size and axial velocity distributions. The system comprised of a 750 mW Argon Ion laser, 57x40 FiberPDA receiving probe, 58n70 FiberPDA detector unit and a 58n10 PDA signal processor, together with transmitting and receiving optics. The sampling rate of the PDA system was 1KHz. For the TRPIV measurements, a 10 kHz pulsing Copper Vapor Laser was used to deliver a sheet of light with an illumination energy of about 5 mJ per pulse. The laser sheet was passed through a cylindrical lens and focused into a vertical plane parallel to the axis of the spray. A Phantom-IV CMOS Camera placed normal to the laser sheet captured the scattering intensity of water spray droplets with pixel resolution of 512x512, a frame rate of 1 kHz, and a total sampling time of 0.4 sec. The magnification, M and f- number, f of the lens were 1.29 (about 18 μm/pixel) and 2.8, respectively.

The experiments are conducted in a non-reacting quiescent environment with water as the working fliud. A full-cone simplex atomizer with FN 13.68, from Delavan Spray Technologies was used. A single case was used for the comparison. The feed line pressure of the spray was

80 psi. The region investigated, shown in Figure 19, was located 7.7cm below and 4.0 cm to the side of the nozzle. The PDA measurements were taken in the center of this region. It should be noted that for the PIV images, the entire 512x512 pixel field of view was not used for the comparison. Because the PDA has a measurement diameter around 1mm, the PIV images were cropped before hand to correspond to the same measurement region. The corresponding velocity in the region of interrogation was determined to be 80-100 m/s.

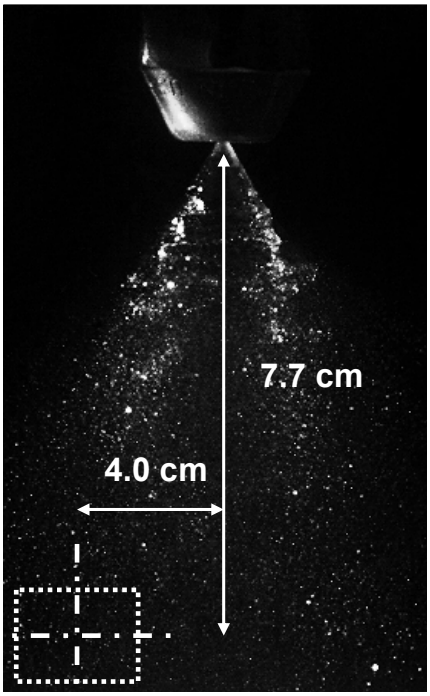

Figure 19– Measurement location of spray

5.2 Experimental Results

Once the images were recorded, a basic threshold filter was used to remove background noise and separate the borders of the particles. It is desirable to se a minimum of image preprocessing to accurately characterize the effectiveness of the subpixel algorithms. A threshold filter was used because it does not modify the intensity values of the pixels. It essentially defines the border around the individual droplets. Subsequently, a recursive nearest neighborhood search associated each droplet with its corresponding set of pixels. The recorded particle image diameter, d_t, was measured for each droplet using the various schemes describe above. The actual droplet diameters were then calculated using Equation 1.

The results of the particle sizing comparison are shown in Figure 20. This histograms show that the continuous four point, and the continuous least squares schemes compare extremely well to the PDA measurements. It is also clear that the standard three and four point Gaussian fits do not perform nearly as well for small particle diameters (8-20 micron range). The three and four point fits do perform well for particle diameters larger than 20 μm. The experimental results support the results of the Monte-Carlo simulations (see Figure 9a). For example, Figure 9a shows a larger bias and RMS errors in the case of the three and four point fits for particle sizes smaller than about five pixels. It should be noted that for the optical setup in this experiment, a particle with a geometric image diameter, d_t, of two pixels, corresponded to a physical diameter, d, of 22 microns. Table 1 shows the mean diameter and standard deviations of these particle size distributions. In all cases, the image based sizing algorithms measured higher mean diameters than the PDA data. The continuous four point and the continuous least squares however only differed by 6% and 3%, respectively.

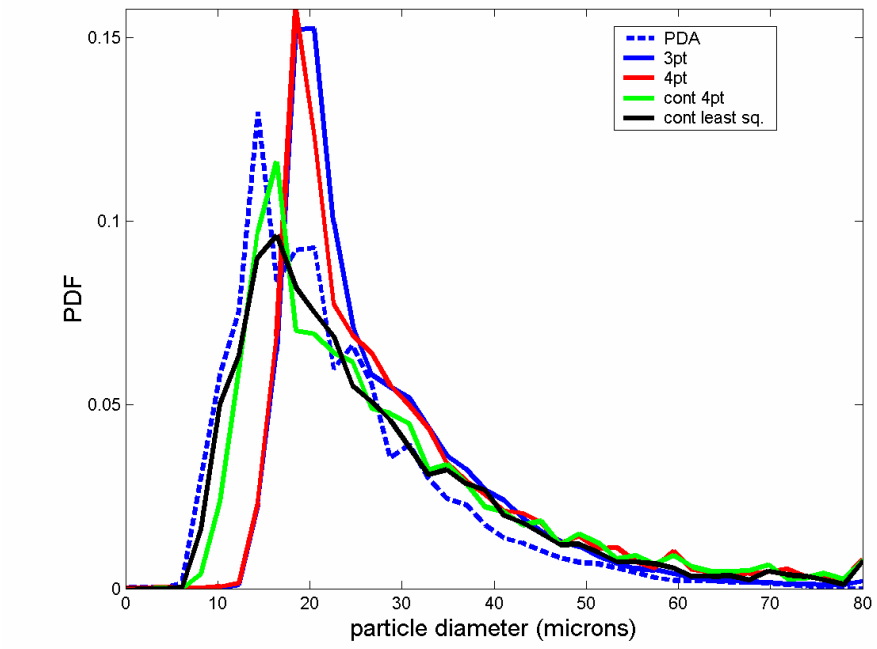

Figure 20 – Comparison of probability density of particle diameters

	mean diameter (μm) / (% err)	standard deviation (μm)
PDA	22.9	11.3
3pt	27.6/21%	11.1
4pt	28.3/24%	12.3
Cont. 4pt.	24.3/6%	13.2
Cont. Least Sq.	23.7/3%	12.7

Table 1 – mean and standard deviation of particle diameters

6 Conclusions

Particle tracking Velocimetry has a profound application in the area of Multi-phase flows. Accurate subpixel sizing and position estimators are required over a large range of particle diameters. Monte Carlo simulations of subresolution particle estimators were carried out to characterize the error of the various schemes. Newly proposed methods, by eliminating the bias error due to pixel discretization, significantly reduced the total error in the diameter compared to the three point Gaussian estimator and the least squares Gaussian estimator, especially for diameters less than 4 pixels. The continuous least squares fit showed a reduction of total error of 60% over both the standard least squares and the three point fit for a random noise level of σ_n =4 and a diameter of 2 pixels. The significant sources of error in calculating particle diameter were found to be random white noise and pixel discretization. Bit resolution was not a significant source of error in the estimation of particle diameter or position. The continuous least squares and standard least squares fits were found to perform equivalently for the calculation of particle position. In addition, both least squares fits were essentially independent of the true particle diameter and significantly reduced the particle position error compared to the other estimation schemes for high particle diameters. The reduction of error for small particle diameters (<3 pixels) was validated experimentally by conducting a high pressure spray experiment. The particle size measurements were compared to a Phase Doppler Analyzer. The continuous least squares and the continuous four point methods differed by only 3% and 6% resprectively with the mean diameter determined with the PDA system. In contrast the three point fit had an error of 21% on the mean diameter. The newly proposed methods provided a significant reduction of error over the current methods for the measurement of particle position and size.

References

Adrian, R., Yao, C. (1985), Pulse laser technique application to liquid and gaseous flows and the scattering power of seed materials, *Applied Optics*, 24.

Bachalo W.D. (1994), Experimental methods in multiphase flows. *Int J Multiphase Flow*, 20, pp. 261-295.

Bachalo W.D., Hauser M.J. Phase/Doppler Analyses for Simultaneous Measurement of Drop Size and Velocity Distribution. *Optical Engineering*, 23, pp. 583–590, 1984

Black, D.L.; Mcquay, M.Q.; Bonin, M.P. (1996), Laser-based techniques for particle-sizing measurement: a review of sizing methods and their industrial applications. *Prog Energy Combust Sci*. 22. pp. 267-306.

Boedec, T; Simoens, S. (2001), Instantaneous and simultaneous planar velocity field measurements of tow phases for turbulent mixing of high pressure sprays. *Experiments in Fluids*, 31, pp. 506-518.

Cowen, E., Monismith, S. (1997), A hybrid digital particle tracking velocimetry technique. *Experiments in Fluids*, 22, pp. 199-211.

Fan, L.S.; Zhu, C., (1997), Principles of Gas-Solid Flows, Cambridge University Press.

Fincham AM; Spedding G. (1997), Low cost, high resolution DPIV for measurement of turbulent flow. *Experiments in Fluids*, 23.

Guezennec, Y.G.; Kiritsis, N. (1990), Statistical Investigation of Errors in Particle Image Velocimetry, *Experiments in Fluids*, 10 pp.138-146.

Jones, A.R., (1999), Light scattering for particle characterization. *Prog. Energy. Sombust. Sci*. 25, pp. 1-53.

Kadambi, J.R.; Martin, W.T.; Amirthaganesh, S.; Wernet, M.P. (1998), Particle Sizing Using Particle Image Velocimetry for Two Phase Flows, *Powder Technology*, 100, pp. 251-259.

Khalitov, D.A.; Longmire, E.K. (1999).Simultaneous two-phase PIV measurements for high speed flows. Third International Workshop on Particle Image Velocimetry. Santa Barbara. Sept. 16-18.

Marxen, M., Sullivan, P., Loewen, M.,Jahne, B. (2000), Comparison of Gaussian particle center estimators and the achievagble measurement density for particle tracking velocimetry. *Experiments in Fluids*, 29.

Nishino, K; Kato, H; Torii, K. (2000), Stereo imaging for simultaneous measurement of size and velocity of particles in dispersed two-phase flow. *Meas. Sci. Tech*. 11 pp. 633-645.

Udrea, D., Bryanston-Cross, P., Lee, W., Funes-Gallanzi, M. (1996), Two sub-pixel processing algorithms for high accuracy particle centre estimation in low seeding density particle image velocimetry. *Optics & Laser Technology*, Vol 28, no 5.

Wang X.S., Wu X.P., Liao G.X., Wei Y.X., Qin J. (2002), Characterization of a water mist based on digital particle images. *Experiments in Fluids*, 33.

Willert, C.E.; Gharib, M. (1991), *Experiments in Fluids*. 10 pp. 181